Geophysical Journal International

Ambient noise multimode Rayleigh and Love wave tomography to determine the shear velocity structure above the Groningen gas field

Journal:	*Geophysical Journal International*
Manuscript ID	GJI-18-1113.R1
Manuscript Type:	Research Paper
Date Submitted by the Author:	n/a
Complete List of Authors:	Chmiel, Małgorzata; Sisprobe, ; Institut des Sciences de la Terre, Mordret, Aurélien; Massachusetts Institute of Technology, Department of Earth, Atmospheric and Planetary Sciences Boué, Pierre; Université Joseph Fourier, ISTerre Brenguier, Florent ; Univ. Grenoble Alpes, ISTerre Lecocq, Thomas; Royal Observatory of Belgium, Seismology - Gravimetry Courbis, Roméo; Univ. Grenoble Alpes, ISTerre Hollis, Daniel; Sisprobe Campman, Xander; Shell International Exploration and Production B.V., ; MIT, ERL Romijn, Remco; Nederlandse Aardolie Maatschappij BV Van der Veen, Wim ; Nederlandse Aardolie Maatschappij BV
Keywords:	Surface waves and free oscillations < SEISMOLOGY, Tomography < GEOPHYSICAL METHODS, Seismic noise < SEISMOLOGY, Wave propagation < SEISMOLOGY, Seismic interferometry < SEISMOLOGY

Ambient noise multimode Rayleigh and Love wave tomography to determine the shear velocity structure above the Groningen gas field

Authors: M. Chmiel[1,2], A. Mordret[3], P. Boué[2], F. Brenguier[2], T. Lecocq[4], R. Courbis[1,2], D. Hollis[1], X. Campman[5], R. Romijn[6], W. Van der Veen[6]

Abbreviated title: Ambient noise multimode Rayleigh and Love wave tomography

[1] Sisprobe, 24 Allée des Vulpains, 38240 Meylan, France.

[2] Institut des Science de la Terre, Univ. Grenoble Alpes, CNRS UMR 5275, Grenoble France.

[3] Department of Earth, Atmospheric and Planetary Sciences, Massachusetts Institute of Technology, Cambridge, MA, USA.

[4] Royal Observatory of Belgium, Seismology-Gravimetry, Avenue circulaire 3, B1180, Brussels, Belgium.

[5] Shell International Exploration and Production, Rijswijk, The Netherlands.

[6] Nederlandse Aardolie Maatschappij B.V., Assen, The Netherlands.

Corresponding author: Małgorzata Chmiel (mchmiel@sisprobe.com)

Dates of submission of the original paper: 10/12/2018

SUMMARY

The Groningen gas field is one of the largest gas fields in Europe. The continuous gas extraction led to an induced seismic activity in the area. In order to monitor the seismic activity and study the gas field many permanent and temporary seismic arrays were deployed. In particular, the extraction of the shear wave velocity model is crucial in seismic hazard assessment. Local S-wave velocity-depth profiles allow the estimation of a potential amplification due to soft sediments.

Ambient seismic noise tomography is an interesting alternative to traditional methods that were used in modelling the S-wave velocity. The ambient noise-field consists mostly of surface waves, which are sensitive to the S-wave and if inverted, they reveal the corresponding S-wave structures.

In this study, we present results of a depth inversion of surface waves obtained from cross-correlation of 1 month of ambient noise data from four flexible networks located in Groningen area. Each block consisted of 400 3C-stations. We compute group velocity maps of Rayleigh and Love waves using a straight-ray surface wave tomography. We also extract clear higher modes of Love and Rayleigh waves.

The S-wave velocity model is obtained with a joint inversion of Love and Rayleigh waves using the Neighbourhood Algorithm. In order to improve the depth inversion, we use the mean phase velocity curves and the higher modes of Rayleigh and Love waves. Moreover, we use the depth of the base of the North Sea formation as a hard constraint. This information provides an additional constraint for depth inversion, which reduces the S-wave velocity uncertainties.

The final S-wave velocity models reflect the geological structures up to 1 km depth and in perspective can be used in seismic risk modelling.

1 INTRODUCTION

For many years it has been shown that seismic noise carries information about the medium and can be used to image the Earth's interior. Studying seismic noise emerged with pioneering work of Aki (1967).

Ambient seismic noise consists of continuous vibrations in the Earth at different frequencies in response to natural processes such as ocean waves and anthropogenic activities such as road traffic. Ambient noise is not flat in the frequency domain, but it peaks near the primary (around 15 s period) and secondary (around 7.5 s period) microseisms and rises at very long periods above 50 s to form a signal now referred to as Earth 'hum' (Ekström, 2001, Rhie & Romanowicz 2004).

At microseismic periods (5-20) s seismic noise is mostly generated by ocean waves and dominated by fundamental-mode Rayleigh and Love waves (Webb, 1998). However, at shorter periods the noise wavefield becomes more complex, with higher modes of surface waves and body waves mixing with fundamental modes (Bonnefoy-Claudet et al., 2006)

Numerous theoretical studies have proved that the cross-correlation of diffuse wavefields (e.g. ambient noise, scattered coda waves) converges towards an estimate of the Green function between the stations (e.g. Weaver & Lobkis 2001, 2004; Derode et al. 2003; Snieder 2004; Wapenaar 2004). In 2004, Campillo and Shapiro demonstrated a practical study showing the possibility of correlating continuous noise recordings to image the Earth's interior.

Noise cross-correlation method has proved useful in imaging the subsurface at local (e.g., Lin et al., 2013, Nakata et al., 2015) and crustal scales (Shapiro et al., 2005, Yang et al., 2007, Lin et al., 2008). Moreover, this method finds applications also in monitoring volcanoes (Sens-Schönfelder and Wegler, 2006; Duputel et al.,

2009; Brenguier et al., 2011), landslides (Mainsant et al., 2013), underground mines (Olivier et al., 2015), geothermal reservoirs (Obermann et al., 2015), and hydrocarbon reservoirs (Mordret et al., 2013, Chmiel et al., 2016).

Surface waves are strongly present in the ambient noise recorded at the surface. Dispersion of Rayleigh and Love waves can be used to obtain a S-wave velocity model, which is essential for different near-surface applications, such as calculating the statics for seismic reflection processing (Mari, 1984), or creating filters to remove ground roll from seismic reflection trace (Halliday et al., 2010). Moreover, the S-wave velocity model plays an important role in estimating seismic risk and site effects related to the amplification of the S-waves (Boué et al., 2016).

In particular, the soft soil responds nonlinearly to the S-wave excitation and develops an amplification of the S-wave (Singh et al., 1988, Beresnev et al., 1995). The shallow sediments or soils can cause amplification and resonances when seismic waves propagate near vertically up to the surface (e.g., Borcherdt and Gibbs, 1976). The S-wave velocity models are commonly used in site characterization for earthquake engineering purposes, for example in the Groningen area (Bommer et al., 2017; Rodriguez-Marek et al., 2017).

The Groningen gas field is one of the largest gas fields in Europe. The long-term gas extraction resulted in a reservoir compaction at depth, and the consequent subsidence results in induced seismic activity (van Thienen-Visser and Breunese, 2015). Even though the magnitude of the earthquakes is quite modest (local magnitudes reported up to ML = 3.6), some of them have strong influence on the surface. It might be related to the complex geological structured of the Groningen field, including the presence of shallow sediment that might amplify the wave motion (Paap et al., 2018).

Recent studies focused on the wave propagation at the Groningen production site in order to assess a potential increase in peak ground acceleration (e.g., Kruiver et al., 2017, Spica et al., 2017, Spica et al., 2018, Paap et al., 2018).

In order to quantify the seismic hazard in the Groningen field, a continuous and temporary data acquisition is performed in the area. In particular, a set of temporary nodal seismic arrays were deployed in the area by the Nederlandse Aardolie Maatschappij (NAM). In this study, we present the results of surface wave inversion to obtain a local S-wave velocity model up to 1000 m depth. We analyse four blocks of around 400 3-components stations, which recorded continuously for one month each. Each block is processed separately, using the same scheme: we first analyse the quality of the recorded data and perform a beamforming analysis. Then, the cross-correlation functions between all stations using all three components are determined to produce nine correlation tensors (ZZ, ZR, ZT, RZ, RR, RT, TZ, TR, and TT). Next, we perform both Love wave and Rayleigh wave tomography. Furthermore, we extract mean phase dispersion curves of the fundamental modes and higher modes of surface waves. Finally, we perform a joint depth inversion of Rayleigh and Love waves with a geological constrain of the inversion (the base of the North Sea formation). The S-wave velocity models in the area of Loppersum, Borgsweer, Scheemda and Nieuw-Scheemda are presented, and finally compared to existing S-wave velocity models of the Groningen field.

2 AMBIENT NOISE RECORD QUALITY

Four flexible VS800 (aiming at obtaining the S-wave velocity model for the first 800 m depth) networks were deployed in the Groningen field, in the northern part of the Netherlands (Figure 1): Loppersum (presented in purple), Borgsweer (presented in

blue), Nieuw-Scheemda (presented in pink) and Scheemda (presented in green). Each data-block consists of around 400 3-C stations with 5 Hz geophones recording ambient seismic noise for one month in 2016 (October-November, Loppersum), and 2017 (December 2016/January 2017, Borgsweer; April, Scheemda; November, Nieuw-Scheemda). The nominal distance between the sensors is ~350m. The inset of Figure 1 shows the geographical position of the Groningen field. In the following, we present the processing workflow using the data from the Nieuw-Scheemda block. The three remaining blocks were processed in the same way.

We first perform the quality check of the data and the analysis of the level of the recorded seismic noise. The level of recorded ambient seismic noise is quite high (Figure 2), similarly to other three blocks.

Figure 2 shows hourly maps (between 16:00h-17:00h, local time) of median noise amplitude calculated over the time period 2017-04-01-2017-05-01 for low frequencies: (1-10) s (a) and high-frequencies: (3-20) Hz (b). Stations 16.014 and 19.026 are indicated with red arrows. Stations located in the proximity of the roads show higher noise levels (e.g., station 19.026). The high-frequency maps show bright spots of high amplitude which aligned with the road position in the area. The low-frequency maps show smaller variations in noise amplitude than the high-frequency maps.

Spectrograms of Z component show the observed vertical seismic noise on raw records throughout the seismic frequency band, and they are presented on Figure 2. Both stations show high level of noise, with the values similar to the high-noise models of Peterson, 1993, although station, 16.014 (Figure 2c) shows lower level of noise and station 19.026 shows higher level of noise (Figure 2d) due to their geographic location. Figure S1, in supplementary material, shows the probabilistic

power spectral density for the station 16.014 (Figure S1a) and the station 19.026 (Figure S1b). It is interesting to notice that after the removal of the instrumental response, we manage to retrieve the signal down to 7 s period, even for the data recorded with 5 Hz nodes.

2.1 Ambient noise beamforming MBIENT NOISE BEAMFORMING

Next, we calculate a daily beamforming analysis by using the Z component of the recorded noise wavefield to reveal the distribution and the dominant direction of the noise source. The frequency-wave number analysis (FK analysis, Rost et al., 2002) allows calculation of the power of the wavefield distributed among different apparent slownesses and back azimuths.

The beamforming analysis computed on the vertical component (Figure 3) of the Nieuw-Scheemda dataset shows a very powerful source of noise coming from the North and the North-West with waves travelling with phase velocities from 500 m/s to 1 km/s or even higher at all frequency bands. Figure 3 also demonstrates the complexity of the Rayleigh waves in the area. The fundamental model of Rayleigh waves is visible at long periods (3-6) s, although as the periods decrease higher modes of Rayleigh waves start to appear (2-4) s and their energy dominate the fundamental mode (0.75-3) s.

The Groningen field lies in the Southern Permian Basin (Whaley, 2009, de Jager and Visser, 2017). The presence of higher-order modes is common in basins (e.g., Boué et al, 2016), and the higher modes are generated in the presence of a velocity inversion in the vertically stratified media, e.g., the upper layer is low enough to cause a complete reflection of both the P-waves and the SV-waves (Heaton 2005). If properly identified, these overtones provide important information on shallow

structures and on the uniqueness of the inverted models (van Heijst and Woodhouse 1997, Chmiel et al., 2018, Spica et al., 2018, Tomar et al., 2018). However, it might be difficult to extract the higher modes of surface waves, due to their interference, simultaneous arrivals, and overlap in the frequency domain. During our analysis of the four data-blocks we observed higher modes of Rayleigh and Love waves at each block, as did Spica et al., 2018 in the Loppersum area. We discuss the overtones extraction in the following sections.

3 NOISE CROSS-CORRELATIONS

The pre-processing steps of obtaining noise-correlation functions and to retrieve the Green's function have become a common procedure in the recent year (e.g., Bensen et al., 2007, Lecocq et al., 2014). Continuous data are first downsampled to 25Hz and then split in to 15 minute segments. Each segment is then spectrally whitened to balance the contributions of all the different sources and to reduce the influence of monochromatic sources. Moreover, each segment with strong energetic patterns (i.e. standard deviation higher than 5 times the standard deviation of the daily trace) is discarded.

The data sections are then cross-correlated with for all the stations pairs. For 403 stations, there are 81003 station pairs. Finally, for each station pair all the 15 minutes cross-correlation are stacked to produce an estimate of the seismic the noise correlation functions (turning all sensor into a virtual source).

The cross-correlation functions contain information at positive and negative lag-times. If the conditions of the noise wavefield are ideal, these signals will be identical due to reciprocity. In the following, we work with the symmetrized noise correlation functions, the mean of the negative and positive lag-times.

4 AVERAGE PHASE VELOCITY DISPERSION CURVES

Figure 4 presents stacked sections of noise cross-correlations filtered in the frequency band (0.5-5) Hz for ZZ (a), RR (b) and TT(c) components. These average seismic sections are constructed by binning the correlations in fixed distance intervals (every 50 m). This procedure is commonly used in order to reconstruct and enhance body waves from correlations (Boué et al., 2013, Nakata et al., 2015). However, this allows us to also explore the multi-modal nature of the surface waves in the Groningen area and to have a better understanding of the general surface wave propagation in the basin. Doing so, we assume that the underlying velocity model is mostly 1D. By stacking the large amount of data in each distance bin, the signal-to-noise ratio (SNR) is highly increased, which permits the extraction of the fundamental mode average propagation characteristics as well as several overtones (when present).

The clear Love wave travels on average with a very slow group velocity of about 300 m/s (Figure 4c). The Rayleigh (Figure 4a and 4b) wave propagation is more complex and shows a high-frequency branch travelling at about 600 m/s and a lower frequency branch travelling on average at 350 m/s.

Next, we perform a frequency-wavenumber (FK) analysis of the stacked sections, to accurately pick phase velocity dispersion curves for the different modes and the different components (Figure 5c). In order to clean up the FK plot and to enhance the maximum of the FK plot, we use multiscale vessel enhancement filtering (Frangi et al., 1998). The dispersion curves are pointed semi-automatically by specifying the control points.

These 1D-averaged phase velocity dispersion curves are presented on 5d (Rayleigh and Love waves). Note that this approach allows a simultaneous measurement of the mean dispersion curves for the fundamental and the 1st higher mode for the Rayleigh waves. The mean group velocity dispersion curves can be calculated as a derivate of the mean phase velocity dispersion curves. We verified that the mean group velocity dispersion curves of calculated from FK plots are coherent with the mean group velocity dispersion curves from frequency time analysis (FTAN) picking. The FTAN measurements of the group velocity are described in the following section.

5 RAYLEIGH AND LOVE GROUP VELOCITY DISPERSION CURVE PICKING AND QUALITY CONTROL

We pick the group velocity dispersion curves for the Love and Rayleigh waves automatically by using the FTAN (Dziewonski et al., 1969) algorithm.

The Love wave group velocity dispersion curves for the 81 003 possible TT correlations have been automatically picked using the FTAN algorithm. We then rejected all the dispersion curves for station pairs separated by less than 1 km to avoid larger uncertainty measurements due to near source effects. Finally, after computing the statistics of all remaining dispersion curves we rejected only the individual points of the dispersion curves larger (or smaller) than the most probable velocity value (called mode) ± 50 m/s. In Figure 5a, the mode value is shown by the blue curve and the 50 m/s limits by the dashed white curves. The background of the figure shows the probability density function of the Love wave group velocity dispersion curves, after the quality control. The extraction was done automatically between 0.5 s and 4.5 s period.

An adequate approach has been applied to ZZ correlations to measure the fundamental mode group velocity dispersion curves. The extraction was done automatically between 1.1 s and 2.9 s of period and 0.2 to 0.5 km/s group velocity. We then rejected all the dispersion curves for station pairs separated by less than 2 km to avoid larger uncertainty measurements due to near source effects and mixing of different modes. In Figure 5a, the mode value is shown by the blue curve and the 50 m/s limits by the dashed white curves. Similarly, to the Love waves, the background of the figure shows the probability density function of the Rayleigh wave fundamental mode group velocity dispersion curves and after the quality control.

We verified the number of dispersion curves left at each period which is used for the surface wave tomography. It goes from 60 000 dispersion curves between at 3.5 s period to about 1000 measurements at 4 s and 30 000 measurements at 0.5 s for Love waves. For Rayleigh waves, the number of dispersion curves left at each period and used for the tomography goes up to measured 3000 dispersion curves for the periods < 3 s. The number of pairs is limited due to the complicated multi-modal nature of Rayleigh waves in the area and complicated shape of the dispersion relation.

The azimuthal distribution of the paths at each inverted period mostly shows the azimuths around North-West are dominating (similarly to the results from the beamforming analysis), but there are still quite a large number of paths in the East-West direction preventing smearing of the seismic anomalies in the tomography. This trend is related to both the noise directivity and the geometry of the array.

6 SURFACE WAVE TOMOGRAPHY

For each period (0.5 to 4.4 s with 0.1 s steps for Love waves, and 1.1 to 2.9 s with 0.1 s step for Rayleigh waves), the dispersion curves are inverted and regionalized into a regular grid of 0.005° by 0.0025° rectangular cells (in longitude and latitude directions) using Mordret et al. (2013) approach. Figure 6 shows the results the Rayleigh wave group velocity maps; the velocities are in km/s. Figure 7 shows the results for the Love wave group velocities.

The density of rays in each cell of the model at each period is of more than 800 rays per cell for Love waves, which permits to achieve a nominal lateral resolution of about 1000 m for all periods for Love waves. The density of rays for Rayleigh waves tomography is lower (200 rays per cell). However, this is still sufficient to ensure an average lateral resolution of about 1000 m for most of the area with a minimum resolution of about 1500 m in the South-West part of the Nieuw-Scheemda area. Moreover, maps for Love and Rayleigh wave show a similar structure at depth. In particular, the maps for Love waves at 2.1 s and Rayleigh waves at 2.5 s show a clear structure from the South to the North, which possibly corresponds to a paleochannel.

7 DEPTH INVERSION AND ESTIMATION OF THE MODEL ROBUSTNESS

The full set of group velocity maps describes local dispersion curves at each single cell of the map. These local dispersion curves can be inverted at depth to obtain local 1D Vs profiles. The ensemble of every best local 1D model will constitute of the final 3D Vs model. We jointly inverted both Love and Rayleigh dispersion curves for robustness. Moreover, we used the mean dispersion curves to complete and improve the inversion at depth. In total, we invert 5 dispersion curves for each single cell. These curves are defined in the Table 1:

Wave type	Velocity	Mode	Periods (s)	Measurement
Love	Phase	Fundamental	0.8-3.5	FK
Love	Group	Fundamental	0.6-4.2	FTAN
Rayleigh	Phase	Fundamental	0.8-2.9	FK
Rayleigh	Phase	1st Higher	0.7-2.9	FK
Rayleigh	Group	Fundamental	1.1-2.9 0.8-1.0	FTAN FK

Table 1: Dispersion curves used in depth inversion for each point of the grid.

The use of phase velocities for both Love and Rayleigh waves and the 1st higher mode of Rayleigh waves in the inversion improves the resolution at depth and lower the uncertainties. Figure S2, in supplementary material, shows sensitivity kernels for group velocities of fundamental mode of Rayleigh and Love waves, Figure S3 shows sensitivity kernels of phase velocities of fundamental mode of Rayleigh and Love waves together with the 1st higher mode for Rayleigh waves. One can see that Rayleigh waves provide the information about the deeper parts of the model, in particular the velocity anomaly at ~ 500 m. Moreover the 1st higher mode of Rayleigh waves adds additional constraint for shallow layers of the model.

For each dispersion curve presented in Table 1, we also define error bars. The error bars of the mean dispersion curves calculated with FK analysis are twice as high as the error bars calculated with FTAN analysis (FK: +/- 100 m/s and FTAN: +/- 50 m/s). This equalizes the contribution of the mean dispersion curves in the inversion.

The depth inversion of surface waves constrains sufficiently the velocity anomalies, although the depth and the topography of different horizons are less well constrained, due to an assumption of the 1D velocity model in the surface wave tomography. This might cause an issue in geologically complex areas, such as the Groningen field, where the structure at depth can be inclined.

In order to constrain better the depth inversion of the surface waves, NAM provided us with a reference of the rock horizon: base of the North Sea (NSB) or Top Chalk formation, which adds an additional constrain to our depth inversion workflow. The NSB horizon was imaged with an active reflection seismic study that was performed in the area Groningen area (e.g., Kuriver, 2017).

First, we extracted the depth of the NSB for the analysed areas. Next, the depth of the NSB was interpolated onto the grid used in depth inversion. The topography of the depth of the NSB is quite flat for the Loppersum and the Nieuw-Scheemda area, although in the Borgsweer area the NSB has a strong topography, showing depth variations between 550-850 m, and in the Scheemda area NSB also varies very strongly, between 400 m and 850 m.

This kind of strong topography occurring at large depths, is hard to resolve with the surface wave inversion, without using any a priori information. We also performed the depth inversion without adding the NSB constrain, and the resulting models shown flat structures at depth, which can be expected with the surface wave inversion, due to the 1D assumption that is used in the group velocity tomography.

We used a Monte-Carlo approach to invert the dispersion curves at depth because of the strong non-linearity of the problem and the absence of accurate a priori starting velocity model. This Monte-Carlo approach is based on a Neighbourhood Algorithm and is described in detail by Mordret et al. (2014). The depth inversion looks for the

optimum parameters at each point of the geographical grid that minimizes the difference between the synthetic dispersion curves and the observed ones. The 1D model is discretized with 32 homogeneous layers with constant thicknesses. During the inversion, the P-wave velocity is scaled to Vs using the empirical relationships of Kruiver et al. (2017) and the density is scaled to Vp using the empirical relationship of Brocher (2005).

The general 1D velocity profile is parameterized by a power-law profile backbone modified by a linear combination of 6 cubic splines for the North Sea. The base of the North Sea formation has a varying depth of +/- 5 m from the provided NSB depth, and has a variable velocity. The top of the Cretaceous has a varying depth and velocity and the velocity profile within the top Cretaceous follows a varying gradient. In total, we invert for 11 parameters: the 6 cubic splines amplitudes and the five previously described parameters. The fifth spline is allowed to have larger amplitude to potentially take into account the presence of the Brussel sands layer (a layer of faster S-wave velocity, e.g., Kuriver et al., 2017). All four data blocks are parametrized in a uniform way.

We sampled a total of 5201 models at each geographical point of our grid. The final model is the average of the 300 best models (with the lowest misfits). This Monte-Carlo technique also allows us to estimate uncertainties for our model as the standard deviation of the distribution of the 300 best velocity models at each depth.

Even if the regionalization phase of the tomography (the group velocity maps computation) involves some lateral smoothing and imposes a minimum correlation length in the maps, the shear-wave versus depth inversion is performed at each pixel independently. Therefore, by using our Monte-Carlo approach for the inversion, we lose the correlation information between neighbouring cells. To overcome this, we

post-process the velocity model by smoothing each layer by a Gaussian kernel the same size as the one used during the group velocity maps computation. This operation induces a damping of the velocity anomaly amplitudes. To correct for that, we measured the standard deviation of the velocity anomalies before and after smoothing and we scale the smooth velocities so that their new standard deviation equates the one of the non-smoothed velocities. The following sections show the final scaled model.

Figure 8a shows the resulting S-wave velocity map for the Nieuw-Scheemda data block (horizontal slice taken at 60 m depth). Figure 8 b-g shows the results of the inversion at depth for one point of the grid (white star on Figure 8a). For each plot, 300 best velocity models are represented in the shade of gray, the best model is represented in color. In Figure 8b-f the error bars are presented for the dispersion curves and in Figure 8g – the final S-wave velocity model is presented in red. We observe that our model achieves a good fit for the five dispersion curves.

The misfit between the measured dispersion curve and the theoretical one is the area of the theoretical dispersion curve outside the area defined by the measured dispersion curve and its uncertainties, normalized by the area of the measured dispersion curve. The details can be found in Mordret et al., 2014.

Figure 9 presents vertical profiles through the 3D S-wave model in the Nieuw-Scheemda area. The location of the profiles is shown in Figure 8a (the black lines). The S-wave velocity model shows an increase of velocity with the depth down to 400 m depth. Below 400 m, the inversion exhibits a high velocity anomaly between 500 and 700 m followed by a low velocity anomaly below 700 m. This anomaly can be identified as, previously mentioned, high velocity layer of Brussel sands. Moreover,

we observe a strong velocity contrast at around 800 m depth related to the presence of the bedrock.

The a priori information about NSB helps to constrain better the depth inversion. The use of NSB depth in inversion strongly improves the resolution and lower the uncertainties of the final model. The velocity uncertainties (calculated as the standard deviation of the best 300 models) of the final model are on the order of 20 m/s above the Brussel sands layer, increasing from surface to depth. The uncertainty is slightly higher in the layer related to the fast velocity layer of the Brussel Sands (Figure S5).

8 DISCUSSION AND COMPARISION WITH EXISITNG MODELS

We now compare our results with an integrated shear-wave velocity model for the Groningen gas field from Kruiver et al. (2017), referred in the following as “Deltares-NAM”. Their Vs model was obtained by integrating high-resolution geological model (first 50 m), field measurements from seismic reflection study and Modal Elastic Inversion (from 50 m to 120 m) and sonic logging (the deepest parts).

Figure 10 shows the comparison between depth slices through the Vs models from Kruiver et al. (2017) with positioned depth slices (at a depth of 65 m) of Loppersum, Borgsweer, Scheemda and Nieuw-Scheemda. Both models are represented in the same colorscale, but slightly different colormaps (see presented colorbars on Figure 10). The models show similar patterns of low and high Vs values, that reveals geological structures (such as paleochannel).

One can see that ambient-noise imaging completes the Vs map from Kuriver et al. (2017) in the areas of Borgsweer and Scheemda, where the active-seismic survey was not available or the Modal Elastic Inversion did not perform well due to the high ambient noise levels. Contrary to this active seismic survey, by using the ANSWT we

are not limited by the source frequency range and we are able to retrieve deeper layers of the area with surface waves propagating at frequencies lower than 1 Hz. Moreover, the dense acquisition allows us to use high-frequency surface wave propagation and in consequence to obtain the shallow layers of the Vs model.

However, we also observe some discrepancies between the two models. In particular, in the eastern corner of the Scheemda data-block, where the topography of NSB becomes strong, we observe an artefact in the S-wave model (Figure S4). This might be related also to a smaller number of dispersion measurements at the edge of the Scheemda data block.

We now compare the 1D average velocity models from all the studied blocks, the “Deltares-Nam” average Vs model (from Kruiver et al., 2017), and the sonic log Vs model provided by NAM for Loppersum and Borgsweer area. It is fair to make this comparison because on the first order, the velocity structures are mainly horizontal with small lateral variations (Figure 11 and Figure 12). Figure 11 shows the comparison between the 1D average velocity models from the depth inversion in all four blocks. Figure 12 shows the comparison between our 1D average velocity models and the “Delaters-Nam” average model for the Loppersum (Figure 12a), Borgsweer (Fibure 12b), Scheemda (Fibure 12c) and (Figure 12d) Nieuw-Scheemda arrays. Our model is presented in colour together with its uncertainty (in grey), Nam-Deltares model is presented in black, and the sonic-log models are presented in red.

The near surface between 50 and 200 m depth is similar for Loppersum, Borgsweer and Nieuw-Scheemda models, and slightly faster (up to 50 m/s) than in Scheemda. Deeper, between 400 m and 700 m depth, all the areas exhibit high velocities due to the Brussel sands. However, the models from Scheemda, Borgsweern Nieuw-Scheemda show higher velocities than the model from

Loppersum (up to 60 m/s). All the models show the strong velocity contrast between 700 m and 800 m depth. For the deep layers, Borgsweer model shows significantly higher velocities, although note that this part of the model has higher uncertainties.

These four models are rather consistent with the 1D Vs models from Deltares-NAM and from the sonic log provided by NAM. The 1D Vs model from the sonic log shows stronger velocity variation (in particular the layer of Brussel sands is shallower and has higher velocities than our 1D models). However, the sonic log is a local measurement, our 1D Vs models are averaged over the whole area.

The discrepancy between the Deltares-NAM models and our models can be spotted for the shallow subsurface.

Deltares-NAM model reveals a low S-wave velocity (Holocene) layer, while our models show higher velocities in the near-surface. It might be related to the limited dispersion measurements in the frequency domain, the parametrization of our depth inversion, and the geometry of the acquisition which limits the measurements of short wavelengths. Also, the discrepancy between the two models grows stronger with depth, which might be related to a lower sensitivity of surface waves to the deeper structures. Moreover, our model consequently shows lower depths of the Brussel sand layer, although the velocities of the Brussel sand layer are in agreement for both models. Finally, the difference between the Deltares model and our 1D average model is within our model's uncertainty range (in grey). Both models show the same depth of the North Sea base at depth 700-800 m, due to the use of a hard constraint in our depth inversion. Finally, the Deltares-NAM model and our VS model show fairly similar crucial features of the model.

Other works also focused on the use of the ambient noise in the Groningen field area. In particular, Spica et al. (2018) used a joint inversion surface waves and

H/V spectral ratio using the Loppersum passive seismic data. Our model shows similar characteristics to Spica's et al. (2018) average 1D velocity model, especially in the first ~500 m. However, their results did not retrieve the Brussel's sands layer due to the weak sensitivity of surface waves at these depths. In this study, we managed to overcome this limitation due to an accurate depth inversion parametrization.

9 CONCLUSIONS

We presented results of a depth inversion of surface waves obtained from cross-correlation of 1 month of ambient noise data from four flexible networks located in Groningen area. Using ANSWT and a joint inversion of Love and Rayleigh waves, we computed high-resolution S-wave velocity models for Loppersumm, Borgsweer, Nieuw-Scheemda and Scheemda area in the Groningen gas field province. Our results prove that with an appropriate processing and parameterization, the surface waves depth inversion can provide detailed S-wave models up to 1 km depth.

The use of phase velocities for both Love and Rayleigh waves, and the 1st higher mode of Rayleigh waves in the inversion lowers the degree of nonuniqueness of depth inversion. Moreover, we were able to image the layer of Brussel sand due to an appropriate parameterization of the depth inversion. The use of NSB as a hard constraint strongly improves the resolution at depth and lowers the uncertainties of the final S-wave model. These improvements allow us to obtain the S-wave velocity models that reflect local geological structures. Final results of the passive survey in the Groningen field area are consistent and complementary with the existing S-wave models.

Our models reveal low and high Vs patterns up to a depth of 1 km and they could be used to model seismic ground motion in order to mitigate seismic risks on the Groningen local population. ANSWT is an interesting alternative to existing methods that are used in modelling shear-wave velocity.

ACKNOWLEDGMENTS

The data were provided by NAM (Nederlandse Aardolie Maatschappij). We thank P. Kruiver from Deltares for providing us with their velocity models. We acknowledge P. Roux, and M. Campillo for useful discussions. The authors thank NAM and Shell for permission to publish. This project received funding from the Shell Game Changer project HiProbe. We also acknowledge support from the European Union's Horizon 2020 research and innovation program under grant agreement No 776622 (PACIFIC). AM acknowledges support from the National Science Foundation grants PLR-1643761.

The processing was done with the help of ObsPy (Krischer et al, 2015) and MATLAB and Statistics Toolbox Release 2017a, The MathWorks, Inc., Natick, Massachusetts, United States.

REFERENCES

Aki, K., 1967. Scaling law of seismic spectrum. J. Geophys. Res., **72**(4), 1217–1231, doi: 10.1029/JZ072i004p01217

Bensen, G. D., Ritzwoller, M.H., Barmin, M.P., Levshin, A.L, Lin, F., Moschetti, M.P., Shapiro, N.M., and Yang, Y., 2008. Processing seismic ambient noise data to obtain reliable broad-band surface wave dispersion measurements. Geophysical Journal International, **169**(3):1239–1260.

Borcherdt, R. D., Gibbs, J.F., 1976. Effect of local geological conditions in the San Francisco bay region on ground motions and the intensities of the 1906 earthquake. Bulletin of the Seismological Society of America. **66**(2), 467-500.

Beresnev, I.A., and Wen, K.L. 1995. P-Wave Amplification by Near Surface Deposits at Different Excitation Levels. Journal of BSSA, **95**(5), 1490-1494.

Bommer, J.J., Stafford, P. J., Edwards, B., Dost, B., van Dedem, E., Rodriguez-Marek, A., Kruiver, P.P., van Elk, J., Doornhof, D., and Ntinalexis, M., 2017. Framework for a ground-motion model for induced seismic hazard and risk analysis in the Groningen gas field, the Netherlands, Earthq. Spectra, **33**(2), doi: 10.1193/082916EQS138M.

Bonnefoy-Claudet, S., Cotton, F., & Bard, P.-Y., 2006. The nature of noise wavefield and its applications for site effects studies: a literature review, Earth-Science Reviews, **79**(3), 205–227.

Boué, P., Poli, P., Campillo, M., Pedersen, H., Briand, X., Roux, P., 2013, Teleseismic correlations of ambient seismic noise for deep global imaging of the Earth, Geophysical Journal International, **194**(2), 844–848, https://doi.org/10.1093/gji/ggt160

Boué, P., Denolle, M., Hirata, N., Nakagawa, S., Beroza, G.C., 2016. Beyond basin resonance: characterizing wave propagation using a dense array and the ambient seismic field, Geophysical Journal International, **206**(2), 1261–1272, https://doi.org/10.1093/gji/ggw205

Brenguier, F., Clarke, D., Aoki, Y., Shapiro, N., Campillo, M., & Ferrazzini, V., 2011. Monitoring volcanoes using seismic noise correlations, Comptes Rendus Geoscience, **343**, 633—638.

Brocher, T., 2005. Empirical relations between elastic wavespeeds and density in the Earth's crust, Bull. Seismol. Soc. Am., **95**, 2081-2092.

Chmiel, M., Roux, P., and Bardainne, T., 2016. Extraction of phase and group velocities from ambient surface noise in a patch-array configuration. Geophysics, **81**, 1–10.

Chmiel, M., Roux, P., Herrmann, P., Rondeleux, B., and, Wathelet, M., 2018. Data-based diffraction kernels for surface waves from convolution and correlation processes through active seismic interferometry, Geophysical Journal International, **214**(2), 1468–1480.

Derode, A., Larose, E., Tanter, M., de Rosny, J., Tourim, A., Campillo, M. & Fink, M., 2003. Recovering the Green's function from field-field correlations in an open scattering medium, J. acoust. Soc. Am., **113**, 2973–2976

Duputel, Z., Ferrazzini, V., Brenguier, F., Shapiro, N., Campillo, M., & Nercessian, A., 2009. Real time monitoring of relative velocity changes using ambient seismic noise at the Piton de la Fournaise volcano (La Réunion) from January 2006 to June 2007, Journal of Volcanology and Geothermal Research, **184**, 164–173.

Dziewonski, A., Bloch, S., and Landisman, M., 1969. A technique for the analysis of transient seismic signals, Bull. Seismol. Soc. Am. **59**(1), 427–444.

Ekström, G., 2001. Time domain analysis of earth's long-period background seismic radiation, Journal of Geophysical Research: Solid Earth (1978–2012), **106**(B11), 26483–26493.

Frangi, A.F., Niessen, W. J, Vincken, K.L., & Viergever, M. A., 1998. Multiscale vessel enhancement filtering. In International Conference on Medical Image Computing and Computer-Assisted Intervention (pp. 130-137). Springer, Berlin, Heidelberg.

Halliday, D., Curtis, A., Vermeer, P., Strobbia, C., Glushchenko, A., van Manen, D.-J., and Robertsson, J.O., 2010. Interferometric ground-roll removal: Attenuation of scattered surface waves in single-sensor data, GEOPHYSICS, **75**(2), SA15-SA25.https://doi.org/10.1190/1.3360948

Heaton, T.H., 2005. Engineering Seismology Notes. http://www.its.caltech.edu/~heatont/Eng_Seism_Notes/ch5_surfacewaves.pdf.

de Jager, J., Visser, C., 2017. Geology of the Groningen field – an overview, Netherlands Journal of Geosciences —doi:10.1017/njg.2017.22.

Krischer, L., Megies, T., Barsch, R., Beyreuther, M., Lecocq, T., Caudron, C., Wassermann, J., 2015. ObsPy: a bridge for seismology into the scientific Python ecosystem. Comput. Sci. Disc. **8**, 014003. https://doi.org/10.1088/1749-4699/8/1/014003

Kruiver, P. P., van Dedem, E., Romijn, R., de Lange, G., Korff, M., Stafleu, J., Gunnink, J. L., Rodriguez-Marek, A., Bommer, J. J., van Elk, J., et al., 2017. An integrated shear-wave velocity model for the groningen gas field, the netherlands, Bulletin of Earthquake Engineering, **15**(9), 3555–3580.

Lecocq, T., Caudron, C., Brenguier, F., 2014. MSNoise, a Python Package for Monitoring Seismic Velocity Changes Using Ambient Seismic Noise, Seismological Research Letters, **85** (3): 715-726. https://doi.org/10.1785/0220130073

Lin, F.-C., Moschetti, M. P., & Ritzwoller, M. H., 2008. Surface wave tomography of the western United States from ambient seismic noise: Rayleigh and love wave phase velocity maps, Geophysical Journal International, **173**(1), 281–298.

Lin, F.-C., Li, D., Clayton, R.W., Hollis, D. , 2013. High-resolution 3D shallow crustal structure in Long Beach, California: application of ambient noise tomography on a dense seismic array, Geophysics, **78**, Q45-Q56, 10.1190/GEO2012-0453.1

Mainsant, G., Larose, E., Bronnimann, C., Jongmans, D., Michoud, C., & Jaboyedoff, M., 2013. Ambient seismic noise monitoring of a clay landslide: toward failure prediction, Journal of Geophysical Research, 117, F01030.

Mari, J.L., 1984. Estimation of static corrections for shear-wave profiling using the dispersion properties of Love waves: Geophysics, **49**, 1169–1179.

Nakata, N., Chang, J.P., Lawrence, J.F., and Boué, P., 2015. Body wave extraction and tomography at Long Beach, California, with ambient-noise interferometry, J. Geophys. Res. Solid Earth, **120**, 1159–1173, doi:10.1002/2015JB011870.

Mordret, A., Landes, M., Shapiro, N. M., Singh, S. C., Roux, P., and Barkved, O. I., 2013. Near-surface study at the Valhall oil field from ambient noise surface wave tomography. Geophysical Journal International, **61**. doi: 10.1093/gji/ggt061.

Mordret, A., Landes, M., Shapiro, N., Singh, S., and Roux, P. 2014. Ambient noise surface wave tomography to determine the shallow shear velocity structure at Valhall: depth inversion with a Neighbourhood Algorithm. Geophysical Journal International, **198**(3), 1514{1525.

Nakata, N., Chang, J. P., Lawrence, J.F., & Boué, P., 2015. Body wave extraction and tomography at Long Beach, california, with ambient-noise interferometry, Journal of Geophysical Research: Solid Earth, **120**(2), 1159–1173.

Obermann, A., Kraft, T., Larose, E., & Wiemer, S., 2015. Potential of ambient seismic noise techniques to monitor the St. Gallen geothermal site (Switzerland), Journal of Geophysical Research: Solid Earth, **120**(6).

Olivier, G., Brenguier, F., Campillo, M., Roux, P., Shapiro, N., & Lynch, R., 2015. Investigation of coseismic and postseismic processes using in situ measurements of seismic velocity variations in an underground mine, Geophysical Research Letters, **42**(21), 9261–9269.

Paap., B., Kraaijpoel, D., Bakker, M., and Nath Gharti, H., 2018, Wave propagation modelling of induced earthquakes at the Groningen gas production site; Geophys. J. Int., **214**, 1947–1960 doi: 10.1093/gji/ggy225

Peterson, J., 1993. Observations and modeling of seismic background noise. U.S. Geol. Survey Open-File Report 93-322, 95 pp.

Rhie, J. and Romanowicz, B., 2004. Excitation of earth's incessant free oscillations by Atmosphere-Ocean-Seafloor coupling, Nature, **431**, 552–556.

Rodriguez-Marek, A., Kruiver, P.P., Meijers, P., Bommer, J. J., Dost, B., van Elk, J., and Doornhof, D., 2017. A regional site-response model for the Groningen gas field, Bull. Seismol. Soc. Am. **107**, no. 5, 2067–2077.

Rost, S., Thomas, C., 2002, Array seismology: methods and applications, Reviews of Geophysics, **40**(3), 8755-1209/02/2000RG000100 1008, doi:10.1029/2000RG000100

Sens-Schönfelder, C., & Wegler, U., 2006. Passive image interferometry and seasonal variations of seismic velocities at Merapi volcano, Indonesia, Geophysical research letters, **33**(21).

Shapiro, N., and Campillo, M., 2004. Emergence of broadband Rayleigh waves from correlations of the ambient seismic noise, Geophysical Research Letters, **31**(7), L07614.

Shapiro, N., Campillo, M., Stehly, L., and Ritzwoller, M., 2005. High resolution surface-wave tomography from ambient seismic noise, Science, **307**, 615–618.

Singh, S. K., Lermo, J., Dominguez, T., Ordaz, M., Espinosa, J. M., Mena, E., and Quaas, R., 1988. The Mexico earthquake of September 19, 1985--a study of amplification of seismic waves in the Valley of Mexico with respect to a hill zone site, Earthquake Spectra, **4**, 653- 673.

Snieder, R., 2004. Extracting the Green's function from the correlation of coda waves: a derivation based on stationary phase, Phys. Rev. E, **69**, 046610.

Spica, Z.J., Nakata, N., Liu, X., Zijian, T., Campman, X., and Beroza, G. C., 2018. The ambient seismic field at Groningen gas field: An overview from the surface to reservoir depth, Seismol. Res. Lett. doi: 10.1785/0220170256

Spica, Z. J., Perton, M., Nakata, N., Liu, X., and Beroza, G. C., 2017. Site characterization at Groningen gas field area through joint surfaceborehole H/V analysis, Geophys. J. Int., **212**(1), 412–421, doi: 10.1093/gji/ggx426.

Tomar, G., Stutzmann, E., Mordret, A., Montagner, J. P., Singh, S. C., & Shapiro, N. M., 2018. Joint inversion of the first overtone and fundamental mode for deep imaging at the Valhall oil field using ambient noise. Geophysical Journal International, **214**(1), 122-132.

Wapenaar, K., 2004. Retrieving the elastodynamic Green's function of an arbitrary inhomogeneous medium by cross correlation, Phys. Rev. Lett., **93**, 254301, doi:10.1103/PhysRevLett.93.254301.

Weaver, R.L., & Lobkis, O.I., 2001. On the emergence of the Green's function in the correlations of a diffuse field, J. acoust. Soc. Am., **110**, 3011–3017.

Webb, S., 1998. Broadband seismology and noise under the ocean, Reviews of Geophysics, **36**, 105–142.

Whaley, J, 2009. The Groningen Gas Field, GeoExPro, **6**(4).

van Thienen-Visser, K., and Breunese, J., 2015. Induced seismicity of the Groningen gas field: History and recent developments, The Leading Edge, **34**(6), 664–671.

van Heijst, H.J., & Woodhouse, J., 1997. Measuring surface-wave overtone phase velocities using a mode branch stripping technique, Geophys. J. Int., **131**, 209–230.

Yang, Y.J., Ritzwoller, M.H., Levshin, A., & Shapiro, N.M., 2007. Ambient noise Rayleigh wave tomography across Europe, Geophysical Journal International, **168**(1), 259–274.

FIGURES

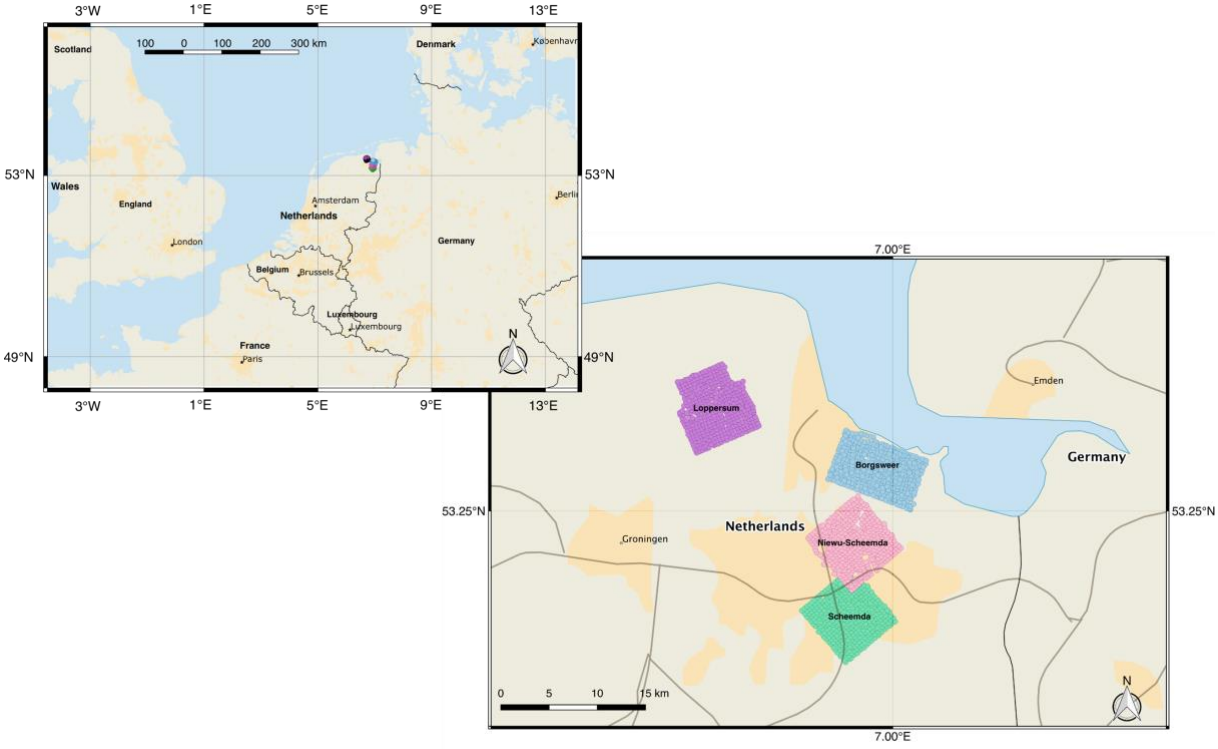

Figure 1: Location of four flexible VS800 networks in the Groningen field, in the northern part of the Netherlands. Four VS800 networks are used in this study: Loppersum (presented in purple), Borgsweer (presented in blue), Nieuw-Scheemda (presented in pink) and Scheemda (presented in green). Each data-block consists of around 400 3-C stations recording ambient seismic noise for a month, and the nominal distance between the sensors is ~350m. The inset shows the geographical position of the Groningen field. In the following, we present the processing workflow using the data from the Nieuw-Scheemda block.

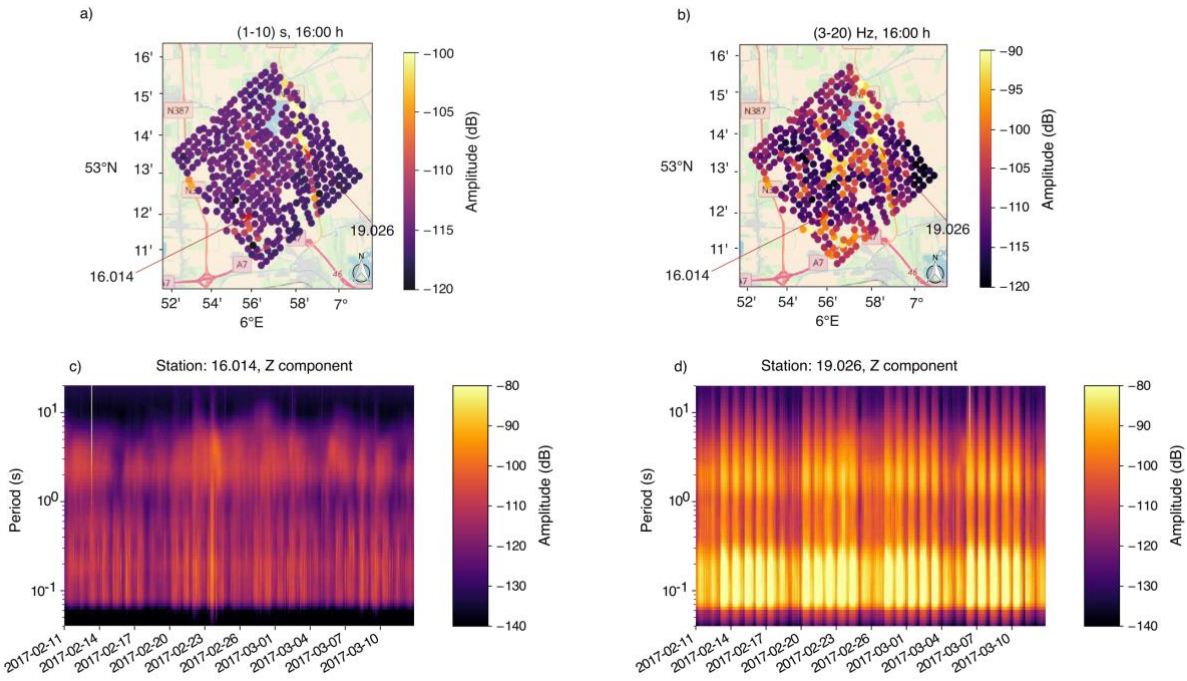

Figure 2: Spectrograms of Z component raw records for stations 16.014 (c) and 19.026 (d), and hourly maps (between 16:00h-17:00h, local time) of median noise amplitude calculated over the time period 2017-04-01-2017-05-01 for low frequencies (a) and high-frequencies (b). Stations 16.014 and 19.026 are pointed with red arrows. Stations located in the proximity of the roads show higher noise levels (e.g., station 19.026). The high-frequency maps show bright spots of high amplitude which aligned with the road position in the area. The low-frequency maps show smaller variations in noise amplitude than the high-frequency maps.

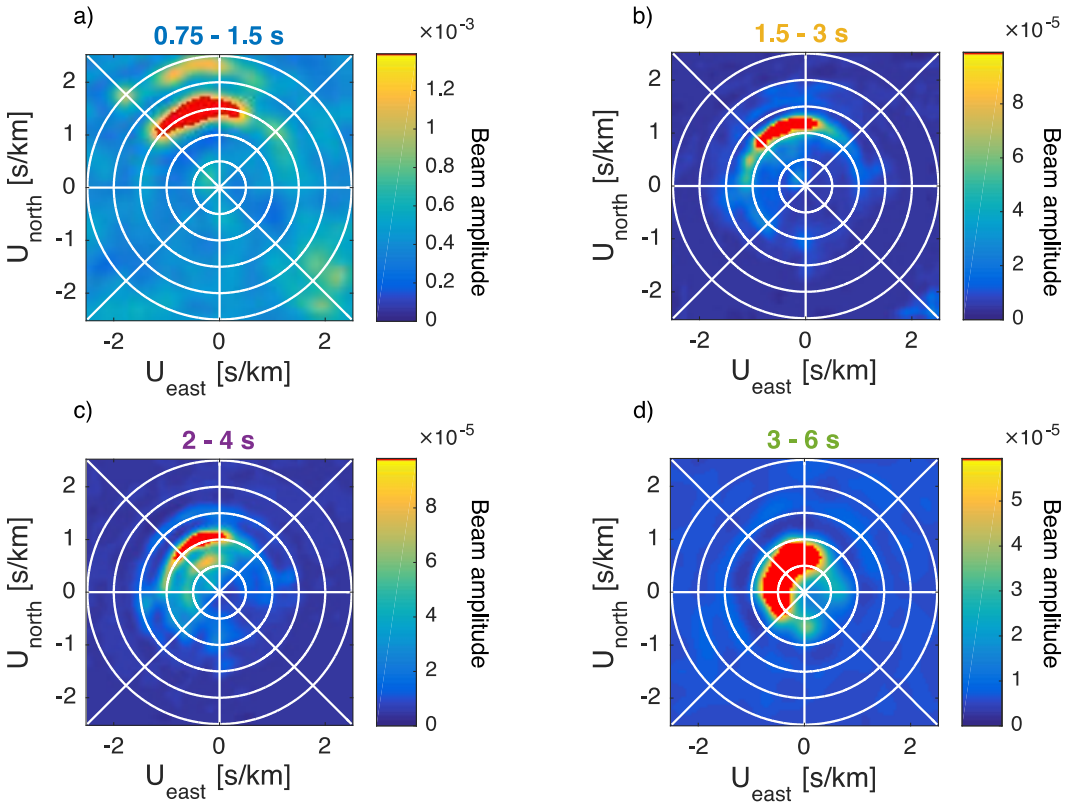

Figure 3: Beamforming results averaged over the monthly acquisition period. Similarly, to the results from other datasets, all frequency bands show a very powerful source of noise coming from the North and the North-West with waves travelling with phase velocities from 500 m/s to 1 km/s or even higher. The fundamental model of Rayleigh waves is visible at long periods (3-6) s in (a), although as the periods decrease higher modes of Rayleigh waves start to appear (2-4) s in (b), and their energy dominate over the fundamental mode (0.75-3) s, in (c) and (d).

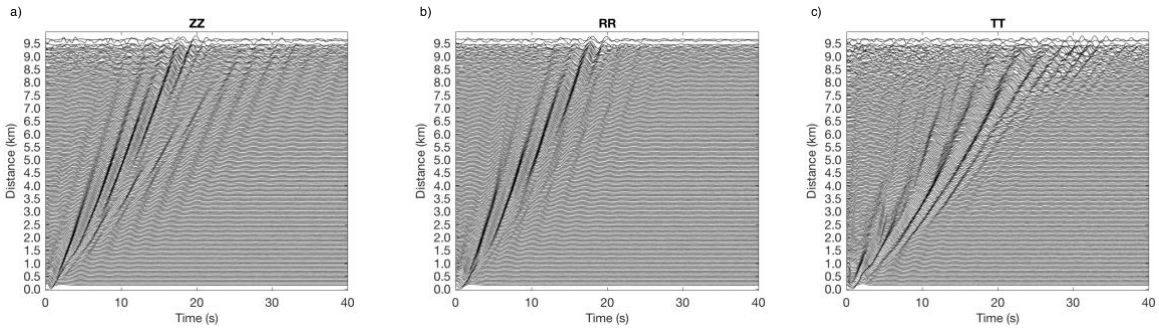

Figure 4: Stacked sections of noise cross-correlations filtered in the frequency band (0.5-5) Hz for ZZ (a), RR (b) and TT(c) components. The fundamental modes and overtones are clearly visible. We build an average seismic section by binning the correlations in fixed distance intervals (every 50 m). By doing so, we assume that the underlying velocity model is mostly 1D. By stacking the large amount of data in each distance bin, the signal-to-noise ratio (SNR) is highly increased, which permits the extraction of the average fundamental mode propagation characteristics as well as several overtones (when present). A frequency-wavenumber (FK) analysis of the stack section allows us to accurately pick phase velocity dispersion curves for the different modes and the different components.

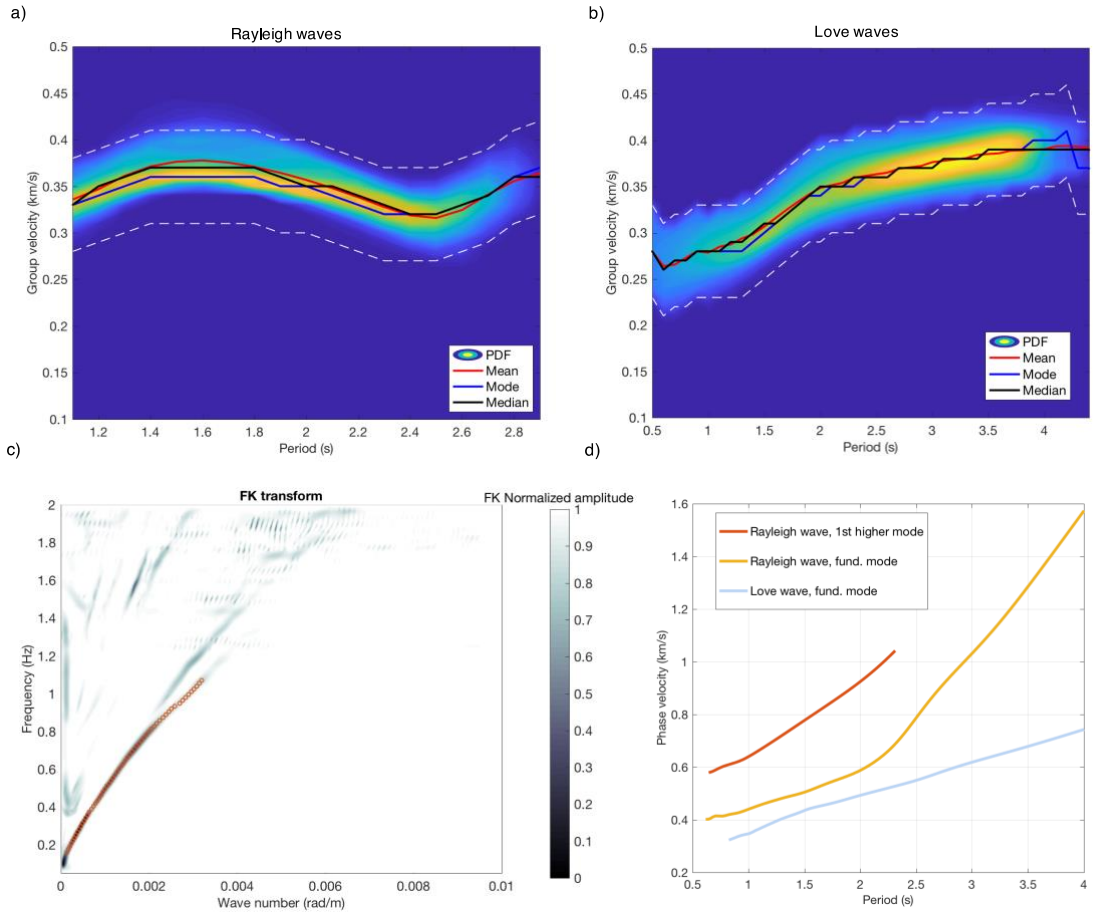

Figure 5: Group velocity and phase velocity dispersion measurements. Probability density distribution of all Rayleigh (a) and Love wave group velocity dispersion curves (b). The red, black and blue curves show the mean, median and most probable dispersion curve, respectively. The dashed white curves are the limits used to reject outlier dispersion curves. (c) FK plot calculated on the stacked sections of noise cross-correlations for TT components. The picked phase dispersion relation of the fundamental mode of the Love waves is presented with orange dots. (d)Mean dispersion curves calculated from F-K plots of Rayleigh waves (fundamental mode in yellow and the 1st higher mode in red), and Love waves (fundamental mode in blue).

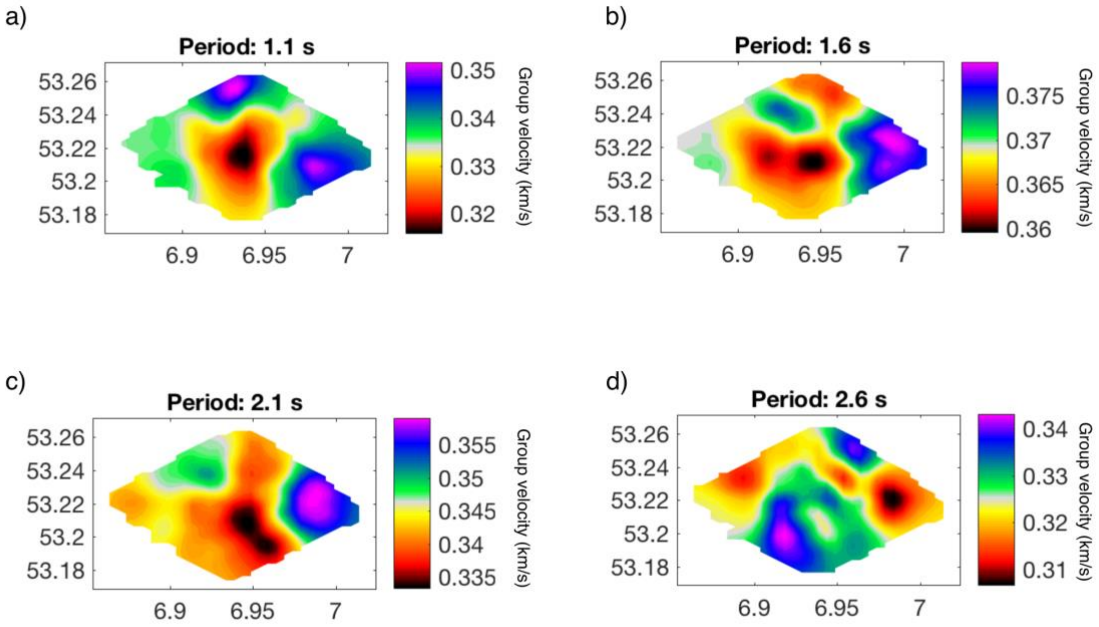

Figure 6: Rayleigh wave group velocities at (a) 1.1 s, (b) 1.6 s, (c) 2.1 s, (d) 2.6 s. For each period (from 1.1 to 2.9 s with 0.1 s step), the dispersion curves are inverted and regionalized into a regular grid of grid 500 m by 250 m rectangular cells (in longitude and latitude directions) using Mordret et al. (2013) approach. The density of ray for Rayleigh waves is of 200 rays per cell. This density is sufficient to ensure an average lateral resolution of about 1000 m for most of the area with a minimum resolution of about 1500 m in the South-West part of the Nieuw-Scheemda block.

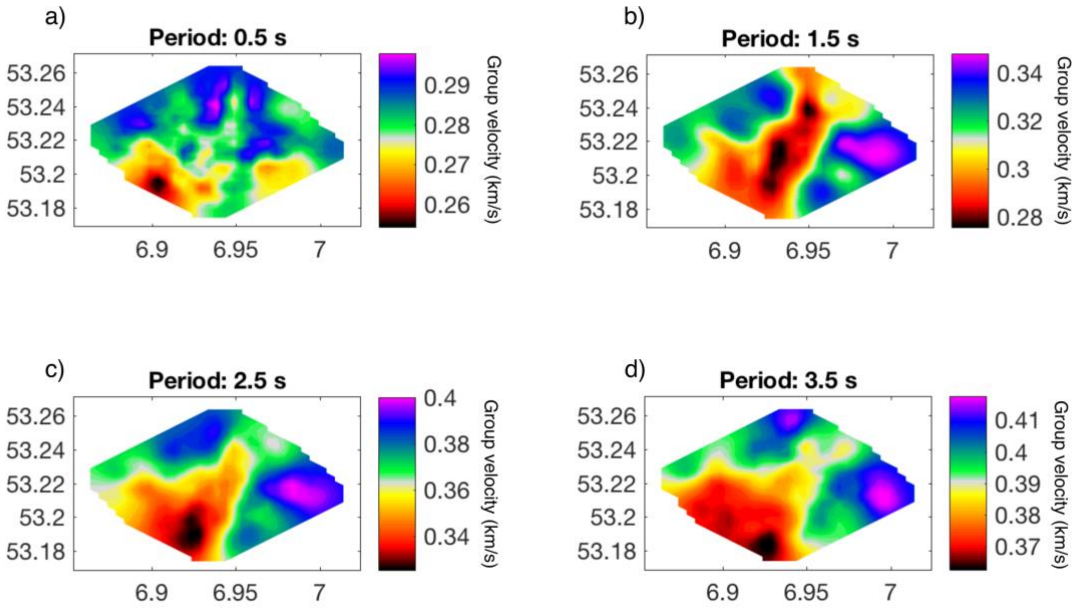

Figure 7: Love wave group velocities at (a) 0.5 s, (b) 1.5 s, (c) 2.5 s, (d) 3.5 s. The dispersion curves were inverted for each period from 0.5 s to 4.4 s with 0.1 s step. The high density of rays of more than 800 rays per cell for Love waves permits to achieve a nominal lateral resolution of about 500 m for all periods for Love waves.

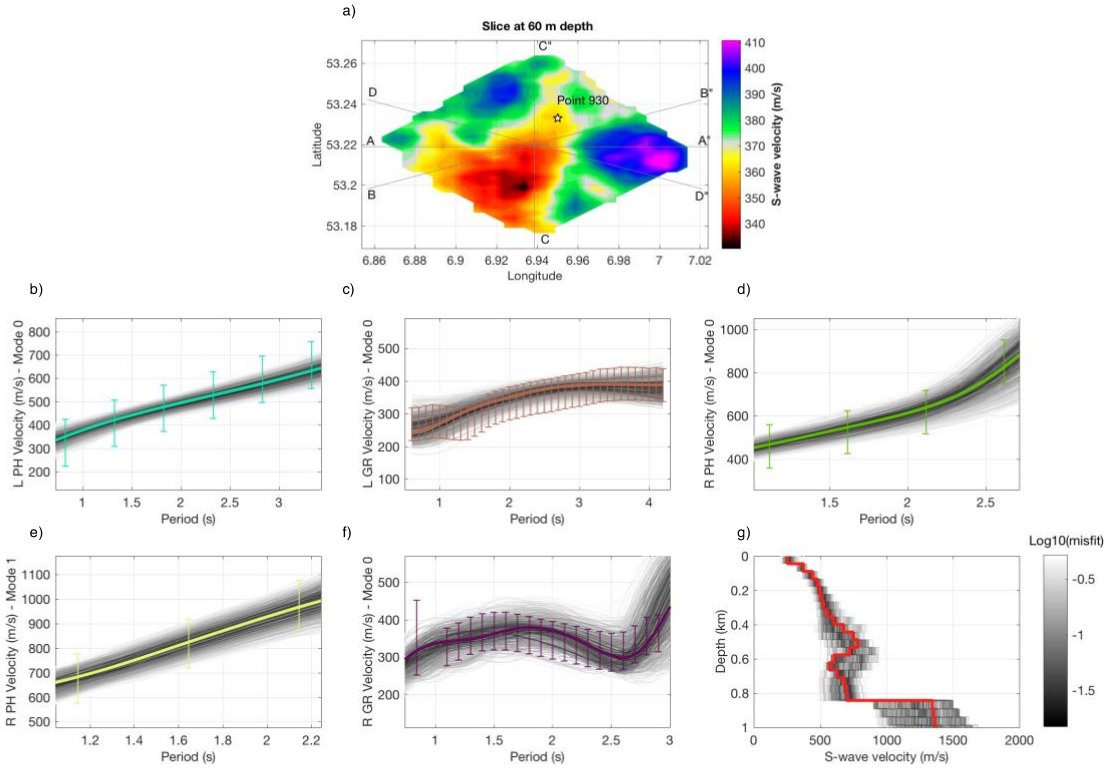

Figure 8: Depth inversion. (a) S-wave velocity map at 60 m with point 930 marked with a white star. Local inversion result. For each plot, 1000 best models are presented in the shade of gray (the scale corresponds to the common logarithm of misfit values), the best model is represented in color. The error bars (dispersion measurements) are presented in the same color. Our model achieves a good fit for the five dispersion curves. The large error bars (100 m/s) are for the average dispersion curves, the small error bars (50 m/s for TT and for ZZ) are for the local dispersion curves. (b-f) Inverted dispersion curves with error bars (all five dispersion curves specified in Table 1 are presented). (g) S-wave velocity model: result of joint inversion of Love and Rayleigh waves. The final VS model is presented in red.

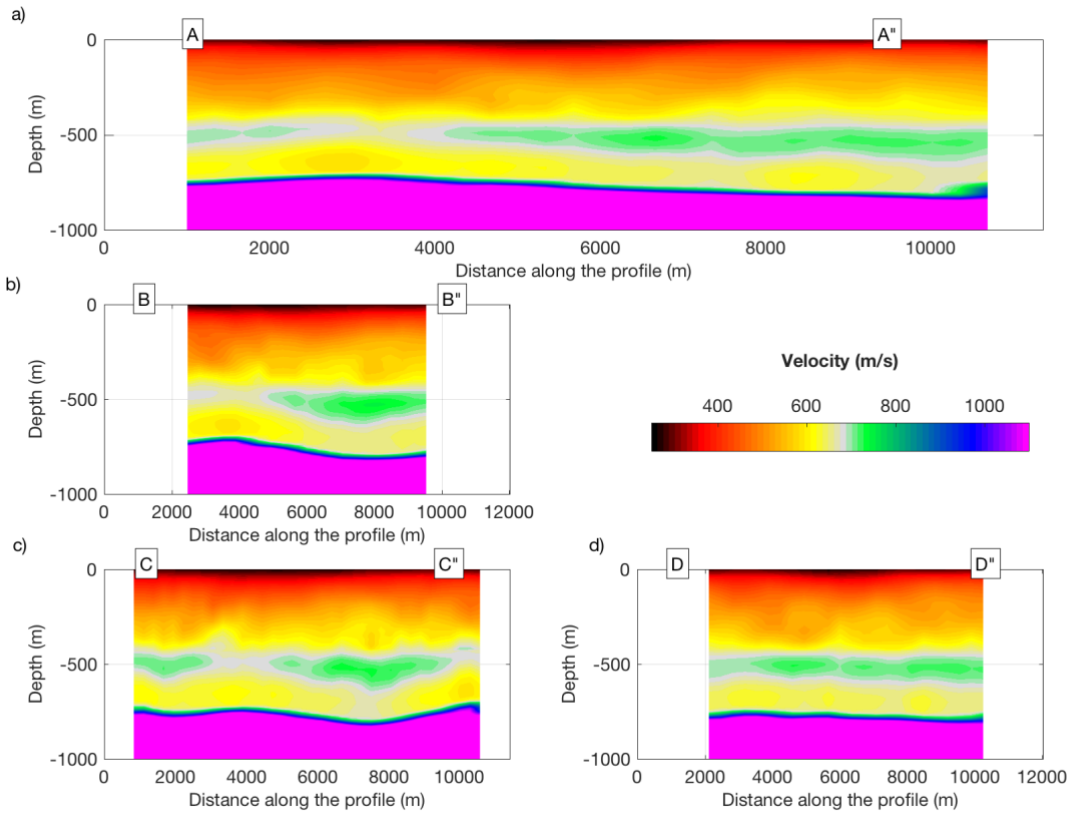

Figure 9: (a-d) Vertical profiles through the 3D model Nieuw-Scheemda. The location of the profiles is shown in Figure 8a.

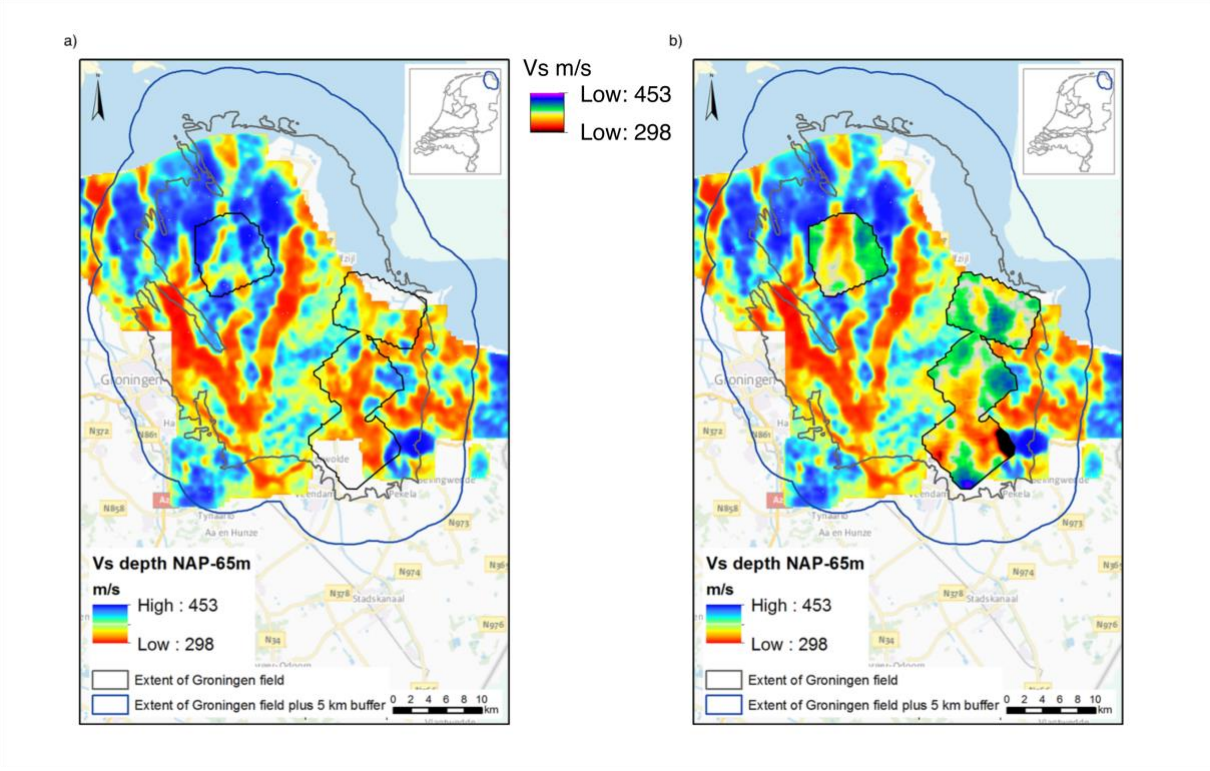

Figure 10: (a) Shear-wave velocity model for the Groningen gas field from Kruiver et al. (2017) with the contours of the four analysed blogs marked in black. (b) Comparison between depth slices through the Vs models from all the data-blocks at a depth of 65 m with the Vs model from Kruiver et al. (2017). The same color scale was used for our results and Kruiver et al. (2017) results. Both maps are presented used the same colorscale, but slightly different colormaps (see presented colorbars).

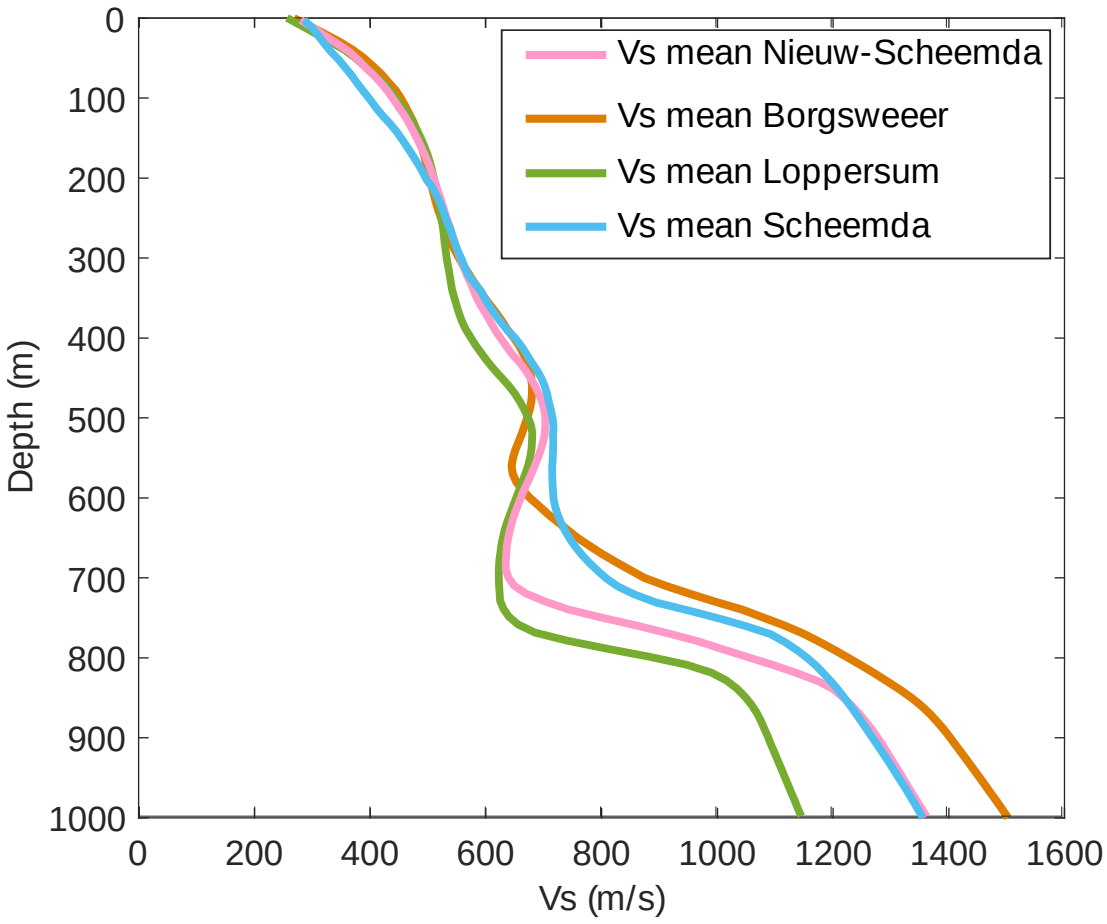

Figure 11: Comparison between the 1D average velocity model from the Loppersum Borgsweer, Scheemda and Nieuw-Scheemda arrays.

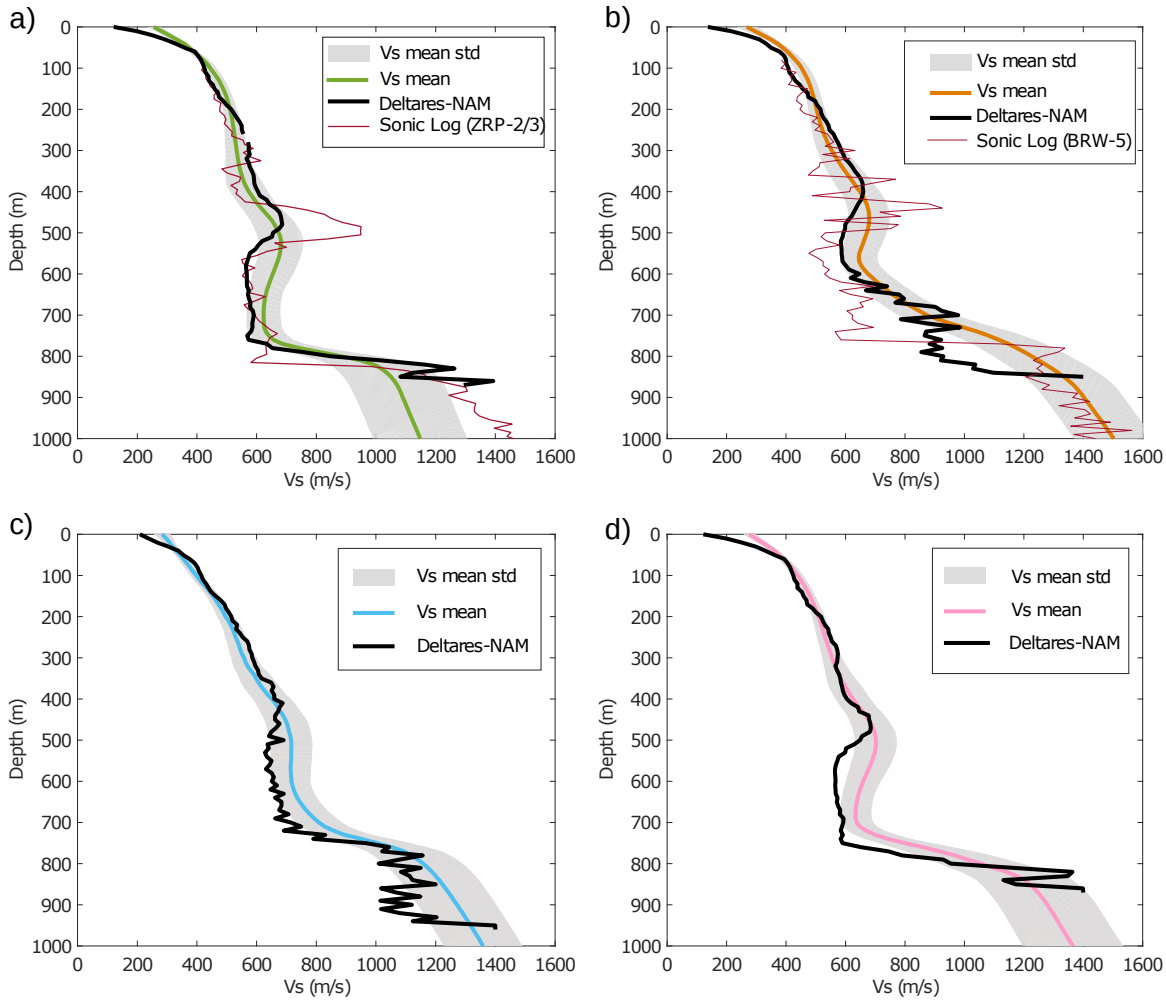

Figure 12: Comparison between the 1D average velocity models from the depth inversion and Deltares-Nam average model for the Loppersum (a), Borgsweer (b), Scheemda (c) and Nieuw-Scheemda arrays (d). For the Loppersum and Borgsweer data-block local sonic-log models are also presented.

SUPPLEMENTARY MATERIAL

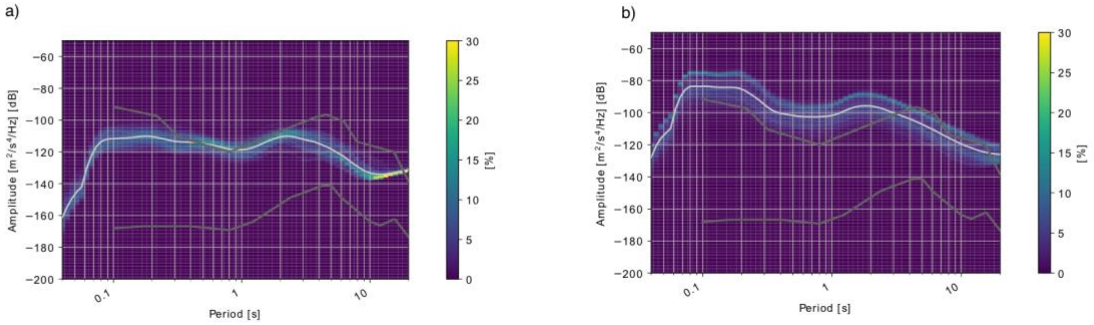

Figure S1: Probabilistic Power Spectral Density (High Noise Model and Low Noise Model are represented in grey lines) for the station 16.014 (a), and the station 19.026 (b). The level of the recorded ambient seismic noise is quite high, and after the removal of the instrumental response, we manage to retrieve the signal down to 7 s period.

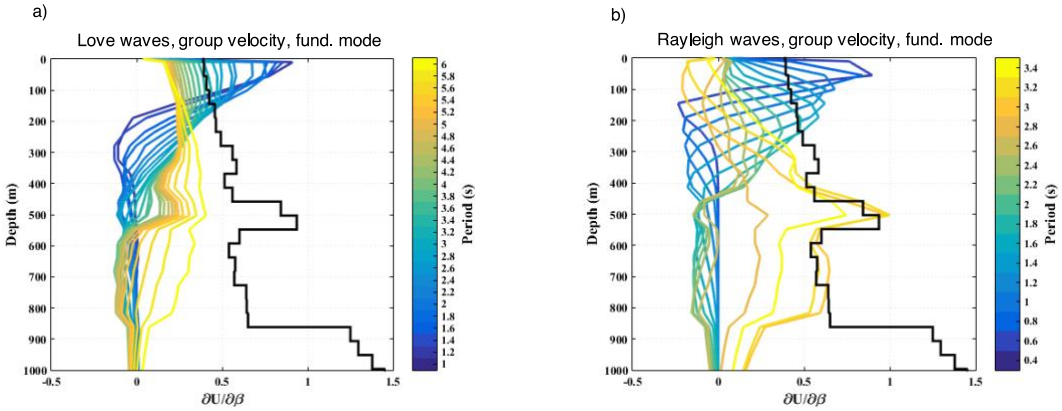

Figure S2: (a) Depth sensitivity kernels for Love wave group velocities, fundamental mode, as a function of depth and period. The black line shows the S-wave velocity model used for the computation and is the sonic log S-wave velocity profile from Loppersum. (b) Depth sensitivity kernels for Rayleigh wave group velocities, fundamental mode, as a function of depth and period.

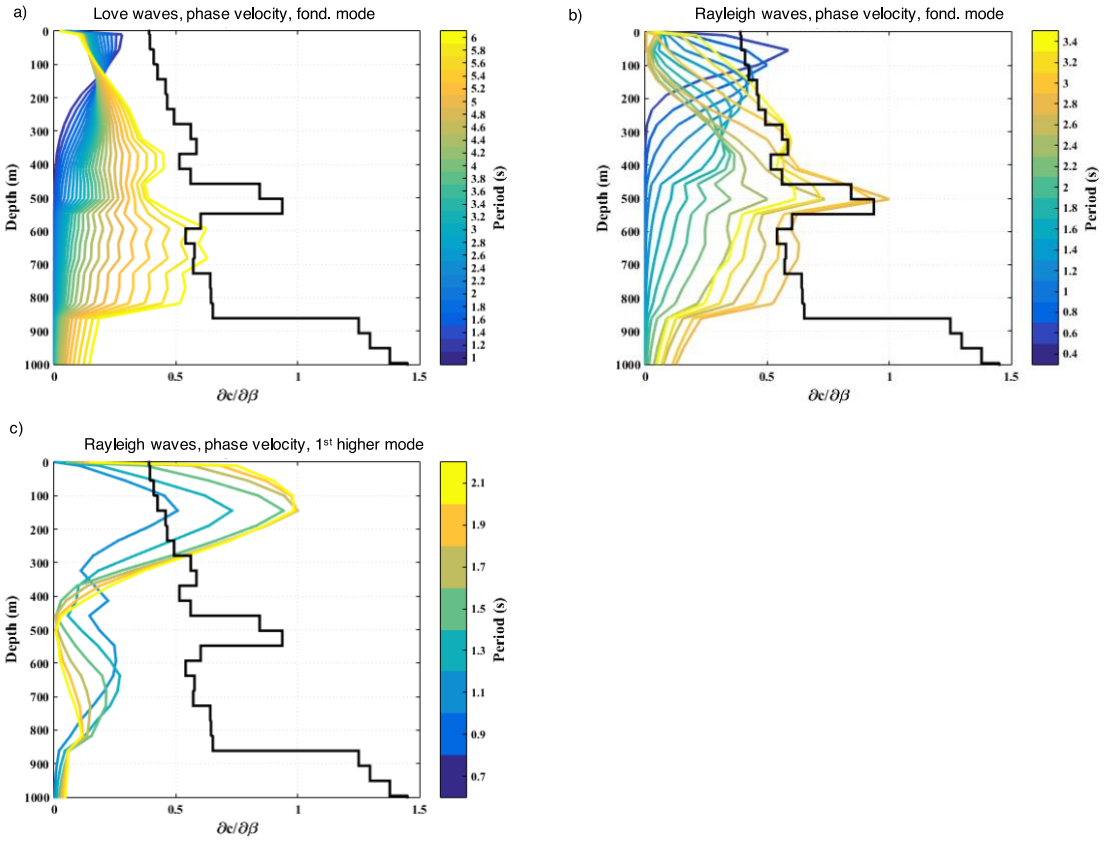

Figure S3: (a) Depth sensitivity kernels for Love wave phase velocities, fundamental mode, as a function of depth and period. The black line shows the S-wave velocity model used for the computation and is the sonic log S-wave velocity profile from Loppersum. (b) Depth sensitivity kernels for Rayleigh wave phase velocities, fundamental mode, as a function of depth and period. (c) Depth sensitivity kernels for Rayleigh wave phase velocities, 1st higher mode, as a function of depth and period.

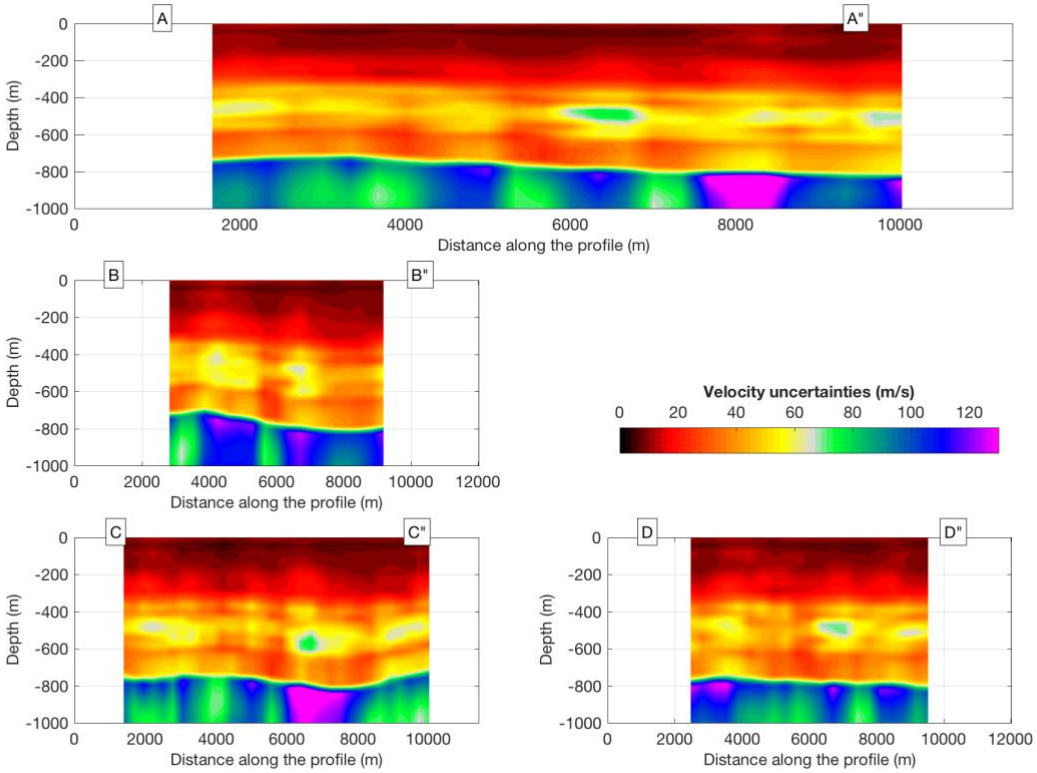

Figure S4: 3D Vs uncertainty model. The locations of the profiles are shown in Figure 8.

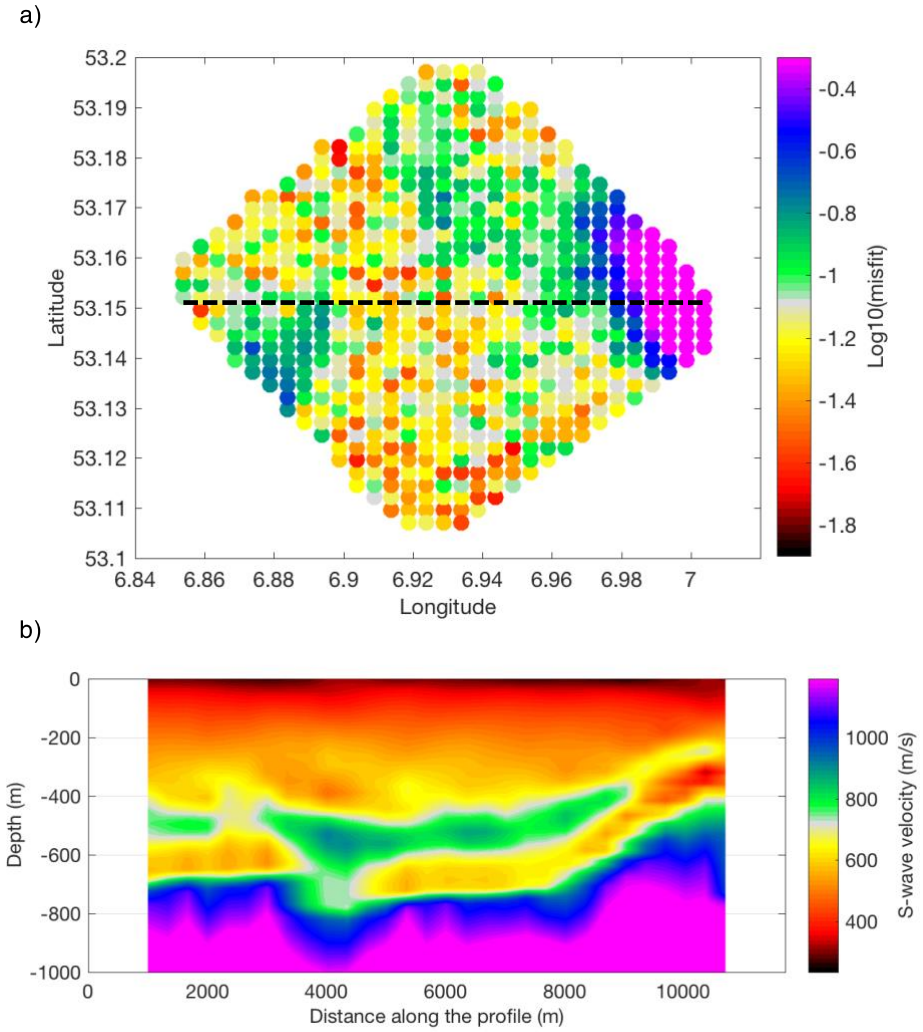

Figure S5: Depth inversion in Scheemda block: (a) the map of the common logarithm of the best misfit. Most of the area exhibits reasonably low misfit (log10(misfit)<0), indicating that the chosen parametrization gives results that fit well the data. However, in the eastern corner of the field, the misfits are anomalously high, demonstrating that the dispersion curves from this area are less well inverted. In this area, the topography of NSB strongly increases. The current parametrization of the depth inversion might be insufficient for this area and the 1D approximation used in surface wave inversion is no longer valid. Moreover, the higher misfit might

be due to a smaller number of dispersion measurements at the edge of the Scheemda block. (b) Vertical profiles through the Scheemda 3D model (marked in dashed line in a).